# Designing CuO–SiO2 and Cu0–SiO2 Monolithic Ceramics Bearing Hierarchical Porosity Toward Robust and Cycling CO Oxidation Properties

Antoine Vardon, Hugo Labarrère, Frédéric Nallet, Nicolas Chanut, François Weill, Christine Labrugère-Sarroste, Jean-Louis Bobet, Isabelle Ly, Florence Epron, Catherine Especel, et al.

Manuscript prepared as a full paper for submission to ***Chemistry of Materials***

# Designing $CuO\text{-}SiO_2$ and $Cu°\text{-}SiO_2$ Monolithic Ceramics Bearing Hierarchical Porosity towards Robust and Cycling CO Oxidation Properties

Antoine Vardon,[1] Hugo Labarrère,[1] Frédéric Nallet,[1] Nicolas Chanut,[2] François Weill,[3] Christine Labrugère-Sarroste,[4] Jean-Louis Bobet,[3] Isabelle Ly,[1] Florence Epron,[5] Catherine Especel,[5,*] and Rénal Backov[1,*]

[1] Université de Bordeaux, CRPP-UMR CNRS 5031, 115 Avenue Albert Schweitzer, 33600 Pessac, France.
[2] Massachusetts Institute of Technology, Department of Civil and Environmental Engineering, 77, Mass. Avenue, Cambridge MA 02139, USA.
[3] Université de Bordeaux, Bordeaux INP, ICMCB-UMR CNRS 5026, 87 Avenue Albert Schweitzer, 33608 Pessac, France.
[4] Université de Bordeaux, PLACAMAT UAR CNRS 3626, 87 Avenue Albert Schweitzer, 33608 Pessac, France.
[5] Institut de Chimie des Milieux et Matériaux de Poitiers, IC2MP-UMR 7285 CNRS - Université de Poitiers, 4 rue Michel Brunet, TSA 51106, 86073 Poitiers Cedex 9 – France.

* Corresponding authors: renal.backov@crpp.cnrs.fr, catherine.especel@univ-poitiers.fr

## Abstract

In a general context of environmental air remediation, copper oxide-based self-standing porous catalysts (MUB-103(x)) and their reduced homologues (Red MUB-103(x)) have been synthesized and studied for the thermo-conversion of CO towards $CO_2$. Catalytic experiments in dried air conditions are revealing that for the non-reduced catalysts increasing the Cu content is diminishing the light-off temperature $T_{50}$ (corresponding to 50% of conversion). The catalytic performances exhibited by the CuO phase dispersed in the silica porosity of the MUB-103(x) samples are the highest reached to date despite the experimental condition penalty in use. After reduction with $H_2$, the native Red MUB-103(x) catalysts offer CO conversion efficiencies significantly further increased leading to a lowering of the $T_{50}$ values equal to at least 100°C. As such, the CO conversion is reaching a $T_{50}$ temperature of 160°C for Red MUB-103(2) with 1.81 wt% Cu, this catalyst displaying a specific rate of 8.6 $mmol_{CO}$ $g_{Cu}^{-1}$ $s^{-1}$ at 175°C, largely higher than those observed to date. The performances of the Red MUB-103(2) sample were evaluated for CO oxidation in humid conditions with the addition of 5 vol% of water vapor in the feed during 4 cycles, leading to the same efficiency when compared with dry experimental conditions, revealing robustness. A drastic increase of the

CO conversion temperature was observed for the 4$^{th}$ cycle, *i.e.* after 8 h under humid conditions. Analyses of the spent Red MUB-103(2) catalyst after 4 cycles reveal a slight oxidation of copper, leading to $Cu_2O$ species. Importantly, after four cycles, the deactivated catalyst was able to partially recover its performance when reactivated through a 2 h reducing treatment under $H_2$ at 400°C.

## 1. INTRODUCTION

Nowadays modern societies have to face three main concomitant challenges, (i) climate remediation, (ii) fossil-free energy generation, (iii) environmentally-safe protein production, the whole configuration under an exponential growth of earth population. Considering the first aspect of environmental remediation, carbon monoxide and NOx abatement are of primary importance as involved both in vehicles and predominantly industrials gas exhausts (cement and stainless steel industries). As a direct consequence, many efforts have been performed on that matter within the last thirty years[1-5] with the tendency of avoiding the use of high cost noble metals (Pt, Pd, Rh, Au), despite their high activity, while employing transitional metals and their oxides as substitute catalysts.[6] Among diverse substituting metals, copper appears as a candidate of choice due to its abundance, lower cost, and chemical properties where both the Cu(I) and Cu(II) oxide species have been proposed as active sites for CO oxidation at relatively low temperatures.[7-9] Later on, 8 nm copper nanoparticles deposited by magnetron sputtering over silica support have been shown to be very effective towards CO abatement both in dry and humid atmospheres where the efficiency is either enhanced through $H_2$ or inhibited though $O_2$ pretreatments.[10] Considering these studies, the synthetic path of both the active sites and supports is of first importance towards tuning particles sizes, accessibility, stability while employing porous-supported media being whatever carbonaceous[11] or inorganic[8-12] and usually solely mesoporous (pore sizes between 2 and 50 nm). One way of generating porous matter bearing hierarchical porosity to facilitate the active sites accessibility is to employ concentrated emulsions as templates leading to

HIPE-based porous materials, HIPE being the acronym for "High Internal Phases Emulsion".[13-15] When focusing on direct emulsions, dispersion of oil-in-water, the hydrophilic continuous phase supports hydrolytic sol-gel process while the oily droplets will be used as macrocellular molds at diameters above 50 nm.[16,17] As the emulsions need a surfactant to stabilize the oil-water droplet interfaces, being above the critical micellar concentration (CMC), this synthetic route is concomitantly offering mesoporosity templated by the lyotrope mesophase in use. When using silica as inorganic support, the $SiO_4$ tetrahedrons random repartition is promoting the so called "microporosity", pore sizes below 2 nm. These Si(HIPE)[17] can further be hybridized when dedicated to heterogeneous catalysis,[18-21] dual-mixed with either titania to reach random lasing properties[22-24] and $CO_2$ photoreduction in volume,[25] or with alumina to promote efficient acidic heterogeneous catalysts.[26] It is also possible to tune the porosity at the mesoscale where SBA15-Si(HIPE) macrocellular monolith-type materials bearing 2D-hexagonal mesoporosity have been obtained recently.[27,28]

In the present study the first binary $CuO_x$-Si(HIPE) and their reduced homologues Cu°-Si(HIPE) monolith-type-foams bearing hierarchical porosity have been prepared. They are labelled hereafter as MUB-103(x) and Red MUB-103(x) once reduced, where the MUB acronym stands for "Materials of the University of Bordeaux". The catalytic properties of such systems have also been investigated in the CO oxidation reaction both under dry and humid conditions while cycling.

## 2. EXPERIMENTAL SECTION

**2.1 Material syntheses**. High purity dodecane (≥ 99%), hydrochloric acid 37wt % (HCl), tetraethylorthosilicate (≥ 99%, TEOS) and copper (II) chloride dihydrate $CuCl_2$. $2H_2O$ were purchased from Sigma-Aldrich. Tetradecyltrimethylammonium bromide (TTAB) was supplied by Alfa Aesar, while dichloromethane ($CH_2Cl_2$, ACS-reagent RPE) was purchased

from Carlo Erba. All the chemicals were used as received without any further purification. Deionized water was obtained using a Milli-Q water purification system. $CuCl_2.2H_2O$ (1.023 g, 0.41 g and 0.205 g) were dissolved in 16 g of a TTAB (35wt %) water solution. Then 5 g of HCl (37wt %) were added prior adding 5 g of TEOS (pH below 0.05). The solution was stirred for 10 minutes both to promote TEOS full hydrolysis and allow partial evaporation of the native ethanol. Then, 37 g of dodecane were emulsified drop by drop into a mortar through a manual stirring. The native direct oil-in-water emulsion was then transferred into several hemolysis test tubes employed as canisters, where the sol-gel process is let to proceed during one week at 25°C. Then the solidified emulsions were pulled out of the canister and let to wash 12 hours in dichloromethane ($CH_2Cl_2$). The wet materials were let dry in a desiccator for one week and further in air during three days. Finally, a thermal treatment was applied to the materials in order to both sinter the silica network, calcine the TTAB surfactant employed as a mesoscopic mold, and promote the copper oxide nucleation and growth. The thermal treatment was applied under atmospheric conditions as follow: a first temperature increase was applied at 2°C/min until 180°C with a 6 hours' plateau followed by a second temperature ramp at 1°C/min to reach 700°C with a 6 hours' plateau. The cooling process was uncontrolled and directed by the oven inertia. Final expected micro-meso-macroporous self-standing monoliths are labeled MUB-103(1), MUB-103(2) and MUB-103(3) while increasing the amount of copper employed for the syntheses (Table 1). For the reduction, the experimental process was as follow: the MUB-103(x) samples were placed in a cylindrical furnace and pure $H_2$ was introduced up until reaching a pressure of 2 bar. Then the samples were vacuumed for 3 minutes. This process was repeated 3 times to ensure the lowest $O_2$ content in the furnace. Then, the samples were submitted to pure hydrogen flow (with a slight over pressure of 1.05 bar) and the temperature was increased to 400°C at 10°C/min. After 1 day, the samples were cooled down to room temperature still under $H_2$ flow. When the

temperature reached 50°C, the hydrogen flow was stopped while maintaining the total pressure at 1.05 bar. Final reduced materials were labeled Red MUB-103(1), Red MUB-103(2) and Red MUB-103(3) while increasing the copper content.

### 2.2 Material Characterizations.

**2.2.1. Scanning Electron Microscopy (SEM)**. The sample was properly broken down and stuck on an aluminum holder and glued with silver paint. Then the fractured surface was metalized with gold / palladium sputtering. SEM images were acquired with a Hitachi TM-1000 tabletop scanning electron microscope operating with a 15 kV accelerating voltage. The Energy-Dispersive X-ray Spectroscopy (EDS) spectra and the mappings were obtained on a ZEISS EVO 50 scanning electron microscope equipped with an EDX EDAX detector. The electronic source was a lanthanum hexaboride tip ($LaB_6$) and the accelerating voltage was 20 kV.

**2.2.2. Small-Angle/Wide-Angle X-ray Scattering (SAXS/WAXS).** X-ray diffraction experiments were done on an XEUSS 2.0 device (XENOCS, Grenoble, FRANCE) with a GeniX3D system (XENOCS. Micro-focus Copper anode source coupled to a FOX3D single reflection mirror) delivering a monochromatic 8 keV beam (Cu Kα radiation, wavelength $\lambda$ = 1.5418 Å). The beam is further collimated by a set of 2 motorized, scatter-less (4-blade) slits. The powdered samples were put into thin glass capillaries (optical path *ca.* 1.5mm), and exposed for typically 2 hours when recording single images, and twice this duration for composite images recorded in the so-called "virtual detector" mode. Data is collected by a two-dimensional DECTRIS PILATUS-300k detector (Baden-Dättwill, SWITZERLAND) placed at sample-to-detector distances of, respectively, 1633 mm (SAXS configuration), and 147 mm (WAXS configuration), giving access to a range of scattering wave vectors q between 0.007 $A^{-1}$ and 3 $A^{-1}$ thanks to the "virtual detector" mode, with a significant overlap (0.1–0.3 $A^{-1}$) between the two configurations. The XEUSS 2.0 device offers a wholly

evacuated flight path, from the downstream end of the mirror to a few centimeters before the detector, including the samples. The 1D diffractograms (intensity *I* vs *q*) are obtained by processing the detector images with the FOXTROT software (collaboration between XENOCS and the SOLEIL synchrotron (Gif-sur-Yvette, FRANCE) SWING beamline team).

**2.2.3 Transmission Electron Microscopy−Transmission Electron Diffraction (TEM−TED).** TEM samples were prepared and observed in the same conditions as reported in ref 29. The diffraction patterns were generated with a TEM FEI Talos F200S 200 kV. Coupled Images and electron diffraction, either selected area electron diffraction (SAED) or nanobeam diffraction (NBD) were obtained on a JEOL 2100 electron microscope equipped with a GATAN Orius 200D camera.

**2.2.4 Thermogravimetric Analysis (TGA).** TGA were performed in air using a TGA 5500 Discovery TA apparatus. The heating rate was set to 5°C $min^{-1}$.

**2.2.5 Elemental analyses.** Elemental analyses have been performed through ICP while using both ICP AES iCAP 6500 DUO and ICP AES iCAP 7400 Radia apparatus.

**2.2.6 Temperature programmed reduction experiments (TPR).** TPR experiments were performed on the MUB-103 materials after calcination in order to obtain information about the nature of their oxides phases. Prior to the TPR, the catalysts were first pretreated *in situ* under inert flow (Ar) for 1 h at 200°C and cooled down to 30°C. The TPR experiments were performed with a 10 vol.% $H_2$/Ar gas mixture (30 mL $min^{-1}$). The temperature range was 30-500°C with a ramp of 10 °C $min^{-1}$ and the temperature was then maintained at 500°C for 1 h. The measurements of the $H_2$ consumption were made in an AutoChem II/Micromeritics apparatus, using a thermal conductivity detector.

**2.2.7 X-Ray photoelectron spectrometry (XPS).** A ThermoFisher Scientific K-ALPHA spectrometer was used for XPS surface analysis with a monochromatized Al-Kα source (hν = 1486.6 eV) and a 400 μm X-Ray spot size. Powders were pressed onto indium foils. The full

spectra (0-1100 eV) were obtained with a constant pass energy of 200 eV, while high-resolution spectra were recorded with a constant pass energy of 40 eV. Charge neutralization was applied during the analysis. High resolution spectra (i.e. C 1s, O 1s, Si 2p, Cu 2p) were quantified using the Avantage software provided by ThermoFisher Scientific. Main attention was paid on the Cu $2p_{3/2}$ spectra to determine copper chemical environment.

### 2.3 Quantitative porosity investigation.

**2.3.1 Gas physisorption experiments.** A Micromeritics 3Flex surface characterization analyzer (Micromeritics Instrument Corp, Norcross, GA) was used for all measurements. Prior to measurement, the samples were activated under secondary vacuum at 110°C for 12 hours. Activation at 350°C for 12 hours was also performed for comparison and led to similar results, indicating that the outgassing procedure was efficient for both temperatures. Argon (Ar) adsorption isotherms measured at 87 K were collected and interpreted using multi-point Brunauer-Emmett-Teller (BET) analysis for surface area determination[30] over the range 0.05–0.30 relative pressure ($P/P_0$) and with an Ar cross-sectional area of 0.143 $nm^2$. The mesoporous surface area has been determined using the Barrett, Joyner and Halenda (BJH) method while the microporous surface area has been estimated by difference between the BJH mesoporous surface area and the BET surface area, assuming that the macroporous surface area is negligible.

**2.3.2 Helium pycnometry**. Materials skeleton densities have been determined through helium pycnometry using a Micromeritics AccuPy 1330 apparatus. The samples were degassed under vacuum at 130°C for 12 hours prior performing the measurement.

**2.3.3 Mercury porosimetry**. Intrusion/extrusion mercury measurements were performed using a Micromeritics Autopore IV apparatus to determine the scaffolds' macrocellular cell characteristics.

**2.4 Catalytic experiments.** The reaction of CO oxidation was performed in a fixed bed tubular reactor with 50 mg of crushed catalyst. The composition of the gas flow injected continuously was the following: CO 11.6 mL $min^{-1}$, $O_2$ 29.0 mL $min^{-1}$, $N_2$ to complete until a total flow rate of 100 mL $min^{-1}$, leading to a $CO/O_2$ ratio equal to 0.4 and a weight hourly space velocity (WHSV) of 120,000 mL $h^{-1}$ $g_{cat}^{-1}$. The temperature in the reactor was increased gradually with a temperature ramp of 5°C.$min^{-1}$ and with steps of 25°C. The effluents at the reactor outlet were analyzed on line under steady-state conditions in a Varian gas chromatograph (GC-3800) equipped with a thermal conductivity detector (TCD) (applied temperatures: 150°C, 50°C and 120°C for the injector, oven and detector respectively). Before the catalytic test, the sample only calcined was activated during 2 hours under an $O_2$-$N_2$ mixture (respective flow rate of 29.0 and 59.4 mL $min^{-1}$) at 500°C (temperature ramp: 10 °C $min^{-1}$). This activation protocol was not performed in the case of the Red MUB-103(x) materials. Some experiments were carried out under humid condition by adding water vapor (5 vol%) to the carrier gas.

## 3. RESULTS AND DISCUSSION

Considering the pH condition in use (pH below 0.05) addressing the sol-gel process, the silica polycondensation is occurring below the silica isoelectric point (pH≈2.1), in a pH range where the inorganic growth will be rather fractal.[31] Under these pH conditions the silica network will expand within the continuous water phase and induce thereby the generation of self-standing monolithic materials (Figure 1A) where the grey/blackish color is increasing when increasing the copper content. The native inorganic polymer due to its fractal nature can accommodate the oil/water interface curvatures, leading to the typical aggregated hollow spheres configuration of the macroporosity (Figure 1B-G).[17] As the pH synthetic conditions are rather acidic, the copper salts will not precipitate as hydroxides or oxo-hydroxides as it

would be the case if employing alkaline polycondensation conditions. This feature will favor homogeneous distribution of the copper precursors within the silica network and thereby homogeneous distribution of the copper oxide species of the native MUB-103 materials, as revealed with EDS investigations (Figure 1H-I). As we can notice with the Figure 1H-J the copper electronic dispersive intensity observed through EDS is evidently increasing from the MUB-103(1) to the MUB-103(3) as the copper content increases.

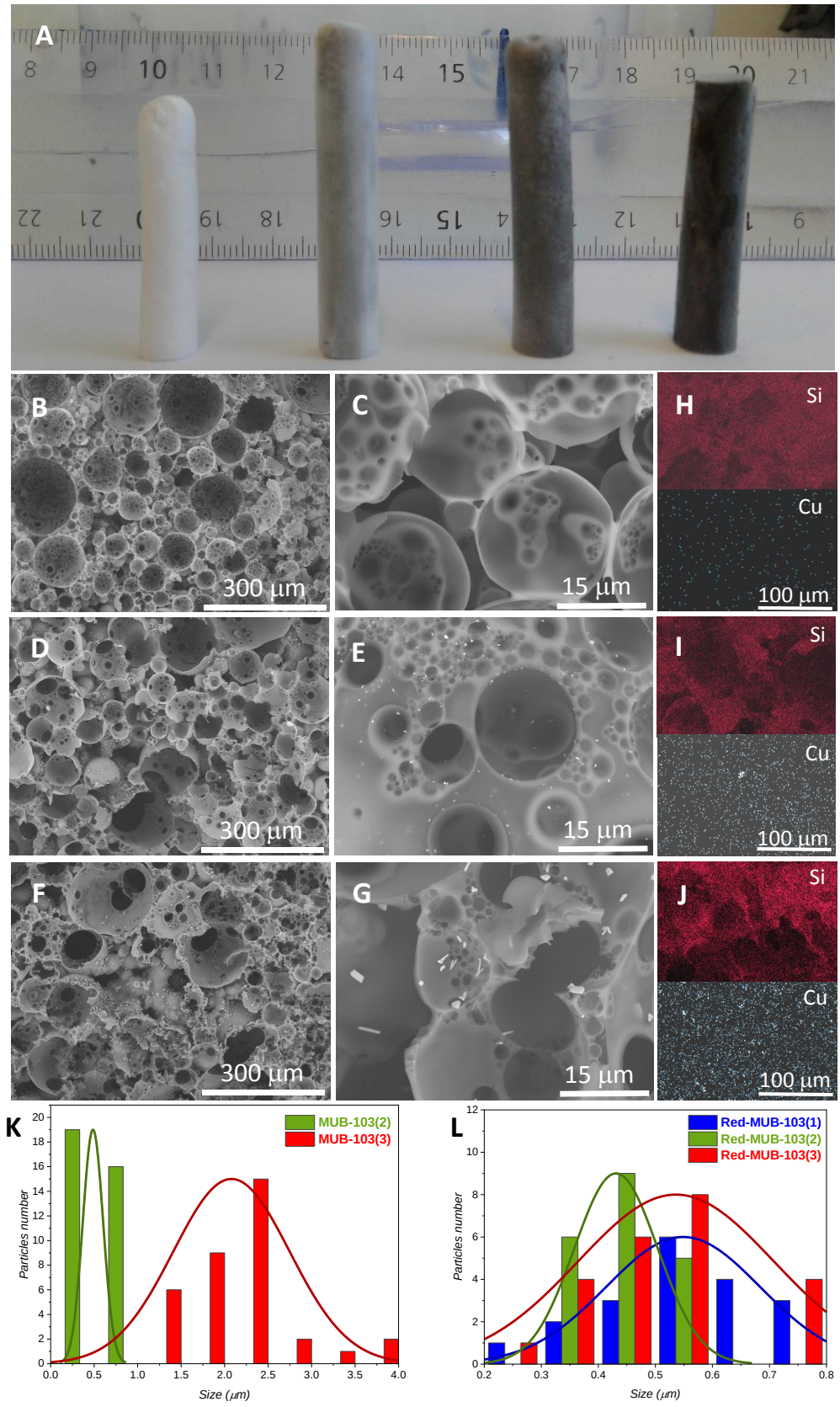


**Figure 1.** Materials observation at the macroscopic length scale. A) Self-standing HIPE materials from left to right bare silica, copper-based MUB-103(1), MUB-103(2) and MUB-103(3) while increasing the Cu amount. B-G) SEM images, B,C) MUB-103(1), D,E) MUB-103(2), F,G) MUB-103(3). H-I) EDS images, H) MUB-103(1), I) MUB-103(2), J) MUB-

103(3), K) CuO crystallite size particle deconvolution for MUB-103 series using the Image J program, L) Cu° crystallite particle sizes deconvolution for Red MUB-103 series using the Image J program. An average of 3.6 $mm^2$ has been investigated for each sample. Standard deviation 0.01 μm.

Considering the Figure 1K, we observe an increase of the particle sizes from MUB-103(1), not detectable under SEM, to MUB-103(3) where the microparticle sizes range falls from 0.25 μm to 4 μm (Figure 1K). Considering the native oxide catalysts, at the macroscopic length scale, the particle sizes are increasing while increasing the copper salt precursor concentration, suggesting that the nucleation events are mostly homogeneous and not occurring heterogeneously at the silica wall interfaces. Indeed, as the sol-gel polycondensation is occurring below the silica isoelectric point,[31] the silica precursors are positively charged,[31] feature that does not favor strong interaction with the $Cu^{2+}$ species as expressed recently with $Co^{2+}$ while dealing with cobalt oxide-based catalysts.[29]

Upon $H_2$ reduction we can first notice that the monolith colors change from grey/blackish for the MUB-103 series (Figure 1) to pink/reddish for the Red MUB-103 series (Figure 1S). Moreover, the macroporous network is depicting still the Si(HIPE) aggregated hollow spheres aggregation (Fig. 1S(b-h)).[17] Being reduced or not, some copper-nanocrystals are bearing elongated shapes while increasing the copper content (Figure 1G and Figure S1b). By performing the $H_2$ reduction treatment, the particle sizes decrease, ranging now from 0.2 μm to 0.8 μm (Figure 1L), except for Red MUB-103(1), bearing microparticles finally detectable under SEM investigations, even bigger than Red MUB-103(2) and in the same range when compared with the Red MUB-103(3). This variation of particle sizes demonstrates that the $H_2$ reduction process is also promoting concomitant matter diffusion where Ostwald ripening occurs for Red-MUB-103(1) material. The Materials stoichiometry can be found in Table 1.

**Table 1**. Elemental analysis data and TGA addressing materials Molar Weight (MW) and stoichiometry. *The $H_2O$ wt% have been found by TGA under air under a heating rate of 5 °C/min. The TGA can be found within the supplemental section (Fig. S2 and Fig. S3). Elemental analyses have been performed using ICP for Copper and Silicon atoms wt% determinations.

| Sample | Cu wt% Found | Cu wt% Cal | Si wt% Found | Si wt% Cal | $H_2O$ wt% Found* | $H_2O$ wt% Cal | MW g $mol^{-1}$ | Proposed Stoichiometry |
|---|---|---|---|---|---|---|---|---|
| MUB-103(1) | 0.54 | 0.56 | 35.2 | 35.2 | 12.01 | 12.45 | 79.46 | $(CuO)_{0.007}(SiO_{1.5}(OH)_{1.0})_{1.0}$. 0.55 $H_2O$ |
| MUB-103(2) | 1.65 | 1.63 | 36.2 | 36.0 | 11.80 | 11.60 | 77.80 | $(CuO)_{0.02}(SiO_{1.6}(OH)_{0.8})_{1.0}$. 0.50 $H_2O$ |
| MUB-103(3) | 5.00 | 4.80 | 33.4 | 32.6 | 20.10 | 19.91 | 85.87 | $(CuO)_{0.065}(SiO_{1.6}(OH)_{0.8})_{1.0}$. 0.95 $H_2O$ |
| Red MUB-103(1) | 0.64 | 0.62 | 39.8 | 39.2 | 2.84 | 2.77 | 71.43 | $(Cu)_{0.007}(SiO_{1.5}(OH)_{1.0})_{1.0}$. 0.11 $H_2O$ |
| Red MUB-103(2) | 1.81 | 1.76 | 39.2 | 38.9 | 4.88 | 4.99 | 72.07 | $(Cu)_{0.02}(SiO_{1.6}(OH)_{0.8})_{1.0}$. 0.20 $H_2O$ |
| Red MUB-103(3) | 5.72 | 5.57 | 38.1 | 37.7 | 3.89 | 3.88 | 74.21 | $(Cu)_{0.065}(SiO_{1.6}(OH)_{0.8})_{1.0}$. 0.16 $H_2O$ |

Still at the macroscopic length scale we have performed mercury porosimetry investigations. First, when considering the Figure 2, we aim at mentioning that the pore sizes distributions are related with the geometry that limits the mercury intrusion, that is to say the connecting windows/throats between adjacent macropores and not the macropores themselves.

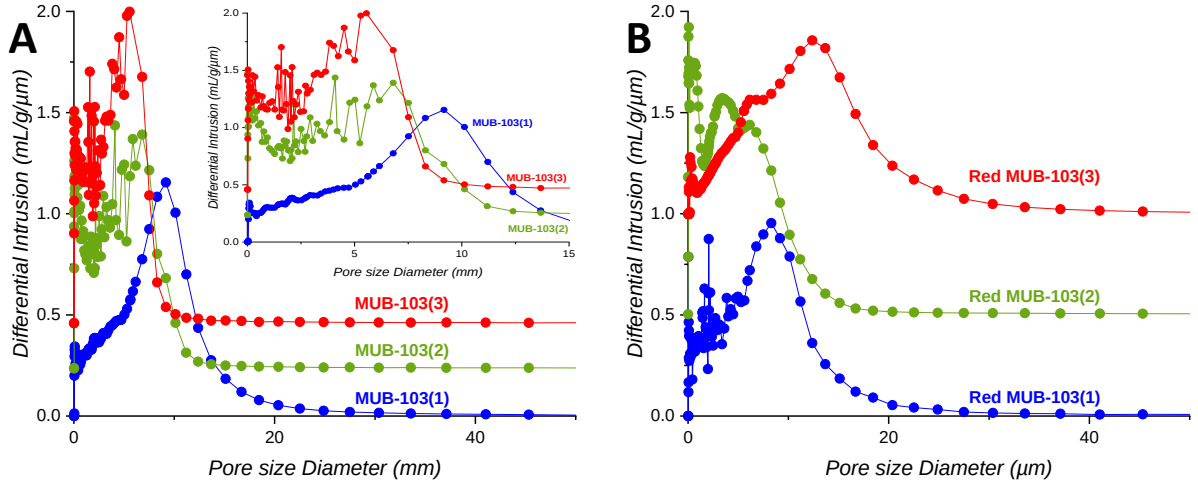


**Figure 2.** Examples of pore sizes distribution obtained through mercury porosimetry. A) MUB-103(1) blue dots, MUB-103(2) green dots and MUB-103(3) red dots, embedded zoom over the pore sizes below 15 µm. B) Red MUB-103(1) blue dots, Red MUB-103(2) green dots and Red MUB-103(3) red dots. For the sake of clarity, the MUB-103(2), the Red MUB-

103(2), the MUB-103(3) and the Red MUB-103(3) curves have been moved upward respectively of 0.5 and 1.0 mL/g/μm.

The connecting windows are falling below 10 μm for the MUB-103(2) and MUB-103(3) materials (Figure 2). Considering the MUB-103(1) material, we can observe still a rather broad pore sizes distributions centered at 10 μm and a shoulder around 4 μm. It means that high copper salt concentration slightly minimizes the starting emulsion coalescence, limiting thus the films' opening and thereby the diameters of the native throats. As copper salt concentration increases, a salting-in effect is rendering the TTAB molecules more soluble and thereby more efficient to stabilize the oil-water interfaces where weak coalescence will be further expressed under the MUB-103(2) and MUB-(3) synthetic paths.[32,33] Additionally we find out that the copper salt is increasing the sol-gel transition kinetic. The higher the sol-gel transition kinetic, the lower the droplets' coalescence. With Figure 2 we can notice that the connecting throats have the tendency to open while applying the reduction treatment. Indeed we notice, as before with cobalt-based MUB series,[29] that the monolith mechanical strength is diminishing while increasing the metal content. The only one feature that would be able to increase the throat diameters through the $H_2$ treatment would be the eroding-induced $H_2$ flux. The lower the mechanical properties the higher the $H_2$ eroding process will be, as it is the case with the Red MUB-103(3) when compared with the Red MUB-103(2) and Red MUB-103(1) bearing lower copper contents.

Aside throat morphologies, mercury intrusions permit reaching the solid foams bulk densities while helium (He) pycnometry, allowing for the determination of the skeleton ones (Table 2). The percentage of porosity has then been determined using the relation (1):

$$\text{Porosity \%} = (1 - \text{bulk density/skeleton density}) * 100 \qquad (1)$$

with Porosity expressed in % and the bulk and skeleton densities in g $cm^{-3}$ (Table 2).

**Table 2.** Bulk density measured by mercury intrusion porosimetry, skeleton density measured by helium pycnometry and calculated porosity using equation (1).

| Sample | Porosity (%) | Skeleton density (g $cm^{-3}$) | Bulk density (g $cm^{-3}$) |
|---|---|---|---|
| MUB-103(1) | 93 | 2.29± 0.01 | 0.087± 0.005 |
| MUB-103(2) | 94 | 2.33± 0.01 | 0.083± 0.005 |
| MUB-103(3) | 95 | 2.38± 0.01 | 0.081± 0.005 |
| Red MUB-103(1) | 96 | 2.37± 0.01 | 0.092± 0.005 |
| Red MUB-103(2) | 96 | 2.45± 0.01 | 0.089± 0.005 |
| Red MUB-103(3) | 97 | 2.53± 0.01 | 0.077± 0.005 |

To get further insights into the nature of the MUB-103 and RED MUB-103 series' porosity, argon adsorption at 87 K have been performed for the determination of their surface area (Figure 3). All the isotherms are bearing a gas up-take at low relative pressure that depicts a degree of microporosity, and a hysteresis (gas capillarity condensation) more or less pronounced at medium relative pressure announcing some mesoporosity. A slight increase of the volume adsorbed in all the adsorption isotherms at high relative pressure is present that is announcing the material's macroporosity. We can notice that the mesoscopic surface areas obtained through Ar physisorption measurements are drastically decreasing from the Si(HIPE) to the MUB-103 and Red MUB-103 series (Table 3), in part, as a consequence of the increase of the materials skeleton density up to 2.53 g $cm^{-3}$ for the Red MUB-103(3) catalyst (Table 2).

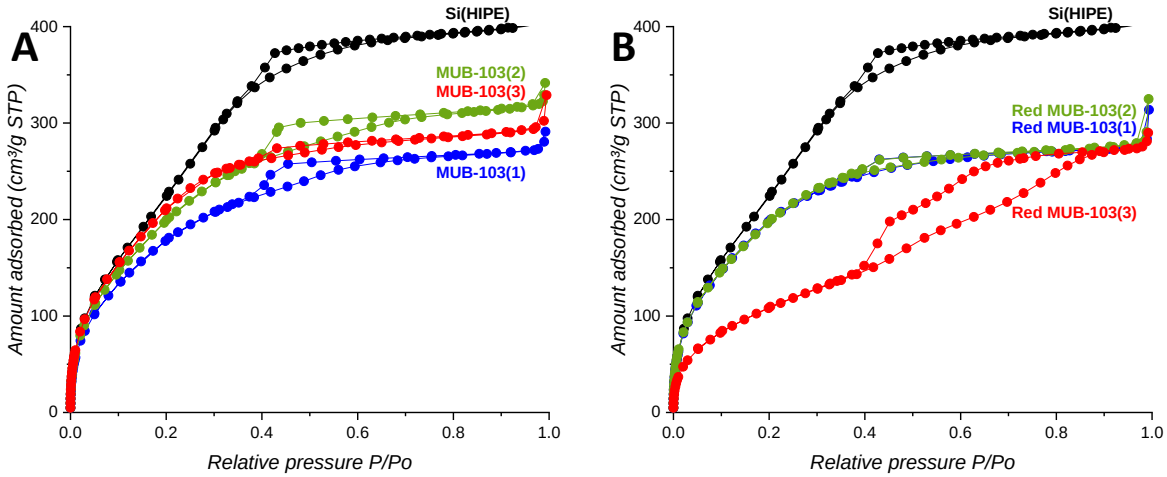


**Figure 3**. Gas physisorption measurements: Ar adsorption-desorption curves. A) MUB-103(1), blue dots; MUB-103(2), green dots; MUB-103(3), red dots. B) Red MUB-103(1), blue dots; Red MUB-103(2), green dots; Red MUB-103(3), red dots. Si(HIPE) curves extracted from ref 29.

Likewise, Ar mesoscopic surface area for the Red-103(3) catalyst is almost divided per two when compared with the ones of other catalysts (Table 3). This drastic decrease of mesoscopic surface area cannot be explained only with a slightly higher skeleton density than the oxides and reduced homologues (Table 2). Also we would like to underline that this decrease of Ar-based mesoscopic surface area is not an artefact of measurement (experiment being reproduced). Indeed the full explanation will come from the TEM investigations as expressed after.

**Table 3.** Surface areas determined using Ar-BET.

| Sample | Ar-BET ($m^2$ $g^{-1}$) | $S_{micro}$ (Ar) ($m^2$ $g^{-1}$) | $S_{meso}$ (Ar) ($m^2$ $g^{-1}$) |
|---|---|---|---|
| Si(HIPE) | 874 | 271 | 603 |
| MUB-103(1) | 635 | 113 | 300 |
| MUB-103(2) | 716 | 300 | 416 |
| MUB-103(3) | 770 | 408 | 362 |
| Red MUB-103(1) | 708 | 379 | 329 |
| Red MUB-103(2) | 701 | 359 | 342 |
| Red MUB-103(3) | 375 | 84 | 291 |

To further investigate the mesoscopic characterization of the materials, TEM studies were performed for the MUB-103 series (Figure 4A, C, E, G) and the Red MUB-103 series (Figure 4B, D, F, H). We can see now that the nanoparticles sizes are decreasing while increasing the copper content. At first glance, this scenario does not make sense thermodynamically speaking. Indeed we have to consider both the SEM (providing the microparticle distributions sizes) and TEM (providing the nanoparticle distribution sizes) to get a systemic explanation. At the micrometer length scale the higher is the precursor concentration the bigger are the growing microparticles (Figure 1K), as higher amount of precursors is consumed in that case towards the nucleation and growth of microparticles, a lower amount of precursors will remain to promote nanoparticles heterogeneous nucleation at the silica walls vicinity minimizing thereby their sizes. Considering this explanation we can understand that, considering the nanoparticle distributions sizes (Figure 4G) the higher is the precursor content the smaller are the nanoparticle sizes observed with TEM (Figure 4).

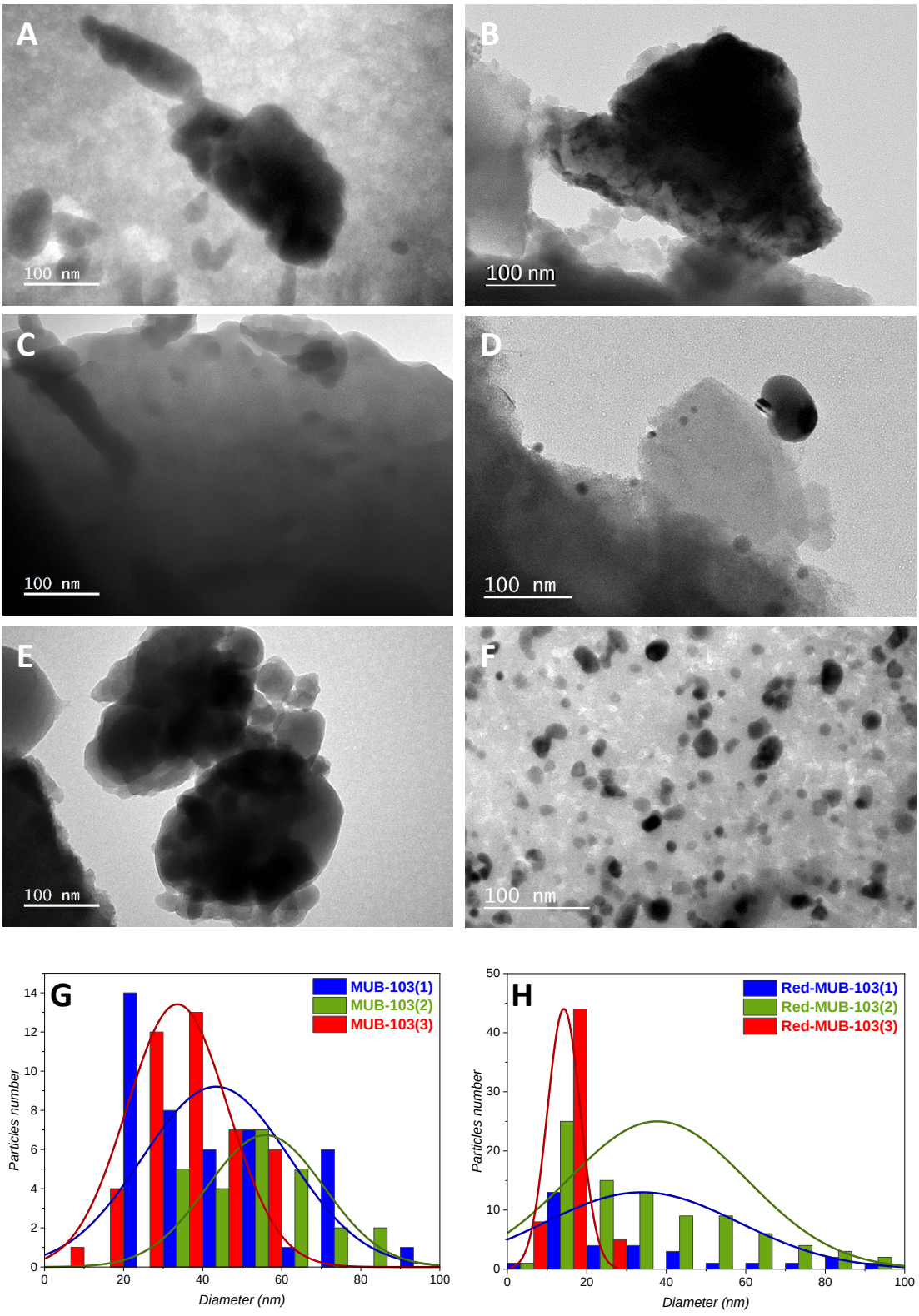


**Figure 4.** Investigation at the mesoscopic length scale through TEM. A) MUB-103(1), B) Red MUB-103(1), C) MUB-103(2), D) Red MUB-103(2), E) MUB-103(3), F) Red MUB-103(3), G) CuO crystallite size particle deconvolution for MUB-103 series using the Image J program, H) Cu° crystallite size particle deconvolution for Red MUB-103 series using the Image J program. An average of 5 $\mu m^2$ has been investigated for each sample. Standard deviation 1.5 nm.

As observed with SEM considering the microparticles, TEM is also depicting a decrease of the nanoparticle sizes through $H_2$ reductive treatment, regardless of the Cu concentration in the materials. As such, under $H_2$ reduction treatment, the average nanoparticle sizes also decrease from 44 nm to 34 nm, 56 nm to 38 nm and 34 nm to 14 nm respectively from the MUB-103(1) to the Red MUB-103(1), MUB-103(2) to the Red MUB-103(2) and MUB-103(3) to the Red MUB-103(3). As the RedMUB-103(3) catalyst is bearing the higher amount and the smaller nanoparticles present at the silica vicinity, these nanoparticles can statistically lock the silica mesoscopic voids, artificially hampering Ar diffusion through the full sample core, providing in that case only an experimental "apparent" lowered Ar surface area, as expressed in Table 3.

SAXS further supports the structural description at mesoscopic scales reached by TEM. As shown in Figure 5, the smaller angle part of the scattering intensity data exhibits the expected power-law decay with exponent -4 (Porod's law)[34] characteristic of clear-cut interfaces—here separating an "outer" empty medium (air) from an "inner" filled medium (silica). The modest, but significant departure from Porod's law, as observed with the MUB-103(3) sample alone, namely an initial decay tentatively described by a power-law with exponent -3.8, is attributed to the presence of numerous copper-rich nanocrystals segregated from the silica matrix, as suggested by the TEM data analyses (Fig. 4g). The structural peak associated to the mesoscopic structure of concentrated worm-like micellar phase used during synthesis is always found in the calcined materials—as especially clear in the Porod representation used in Figure 6. Kind of a "second order" peak, notably for the reference Si-(HIPE) sample, as well as for MUB103-(1), remains visible in all cases but, presumably owing to disorder, it does not fall strictly at the ratio expected for a 2D hexagonal structure, *i.e.*, $\sqrt{3}$.

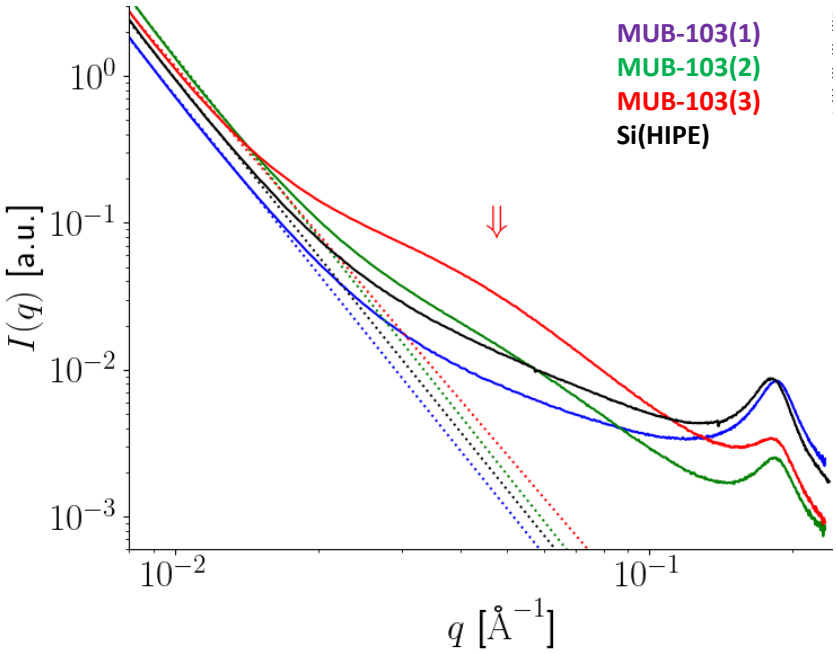


**Figure 5**. Small-angle scattering intensities (double logarithmic scale) for the reference Si-(HIPE) sample (black), and the three MUB-103(1) (blue), MUB-103(2) (green) and MUB-103(3) (red) samples. The coloured dotted lines correspond to power-law decaying intensities with exponents close to -4 (Porod's law) except for the MUB-103(3) sample where the exponent is slightly larger, *i.e.* about -3.8. Note the presence at about 2π/130 1/Å (downwards double arrow symbol), and clearly noticeable for MUB-103(3) only, of a broad feature possibly associated to the presence of CuO nanocrystals.

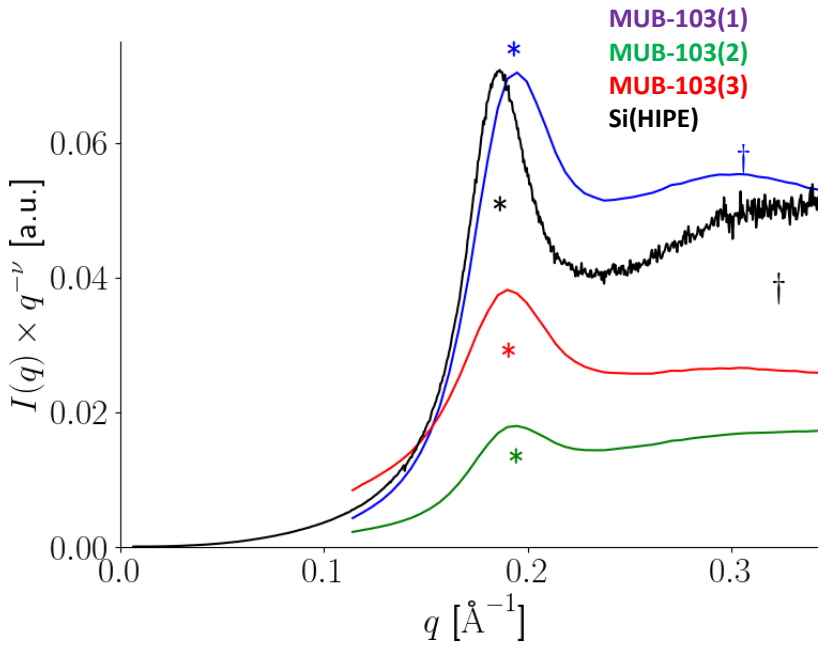


**Figure 6**. Porod-like representation of the small-angle intensities scattered by the calcined materials, emphasizing the mesoporous structure of the reference SI-(HIPE) sample (black), and of the three MUB-103(1) (blue), MUB-103(2) (green) and MUB-103(3) (red) samples.

Exponents ν close to -4 as expected from Porod's law, except for the MUB-103(3) sample where the value is slightly larger, *i.e.* about -3.8. The coloured star marks the location q* in reciprocal space of the characteristic structural peak from the concentrated worm-like micellar phase used during synthesis. Note that for the reference Si-(HIPE) sample a "second order" peak may be found at roughly √3 the "first order" peak (dagger symbol)—as expected for hexagonal 2D order. A "second order" (dagger symbol at √5/2 the "first order" peak) is also clearly observed for the MUB-103(1) material. Associated structural parameters (derived from 2π/q*): SI-(HIPE) 3.36 nm, MUB-103(1) 3.24 nm, MUB-103(2) 3.22 nm, MUB-103(3) 3.29 nm.

At the microscopic length scale, WAXS investigations have been performed (Figure 7).

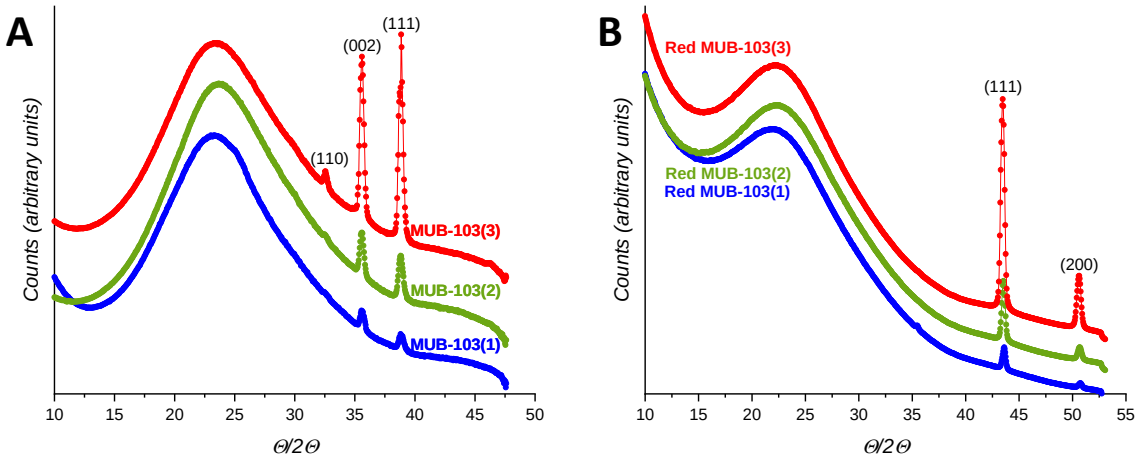


**Figure 7.** WAXS investigation**.** A) MUB-103(1) blue dots, MUB-103(2) green dots and MUB-103(3) red dots. (110), (002) and (111) main diffraction peaks of the CuO monoclinic structure with space group C2/c, (JCPDS card No. 47-1049). B) Red MUB-103(1) blue dots, Red MUB-103(2) green dots and Red MUB-103(3) red dots. (111) and (200) main diffraction peaks of the Cu° face centered cubic structure (JCPDS Card No. 85-1326).

Considering the MUB-103(x) series the WAXS spectrum depict the typical (110), (002) and (111) (h, k, l) diffractions patterns of the tenorite CuO monoclinic structure (JCPDS card No. 47-1049), in total agreement with XPS investigation (Figure 8A bottom, Figure S4 and Figure S5). When performing the $H_2$ reducing treatment we can see that these diffraction peaks vanish completely while are appearing the (111) and (200) Miller indices peaks of the Cu° face-centered cubic (JCPDS Card No. 85-1326). Either for the oxides MUB-103 or their

reduced analogues, diffraction peak intensities are increasing with the copper contents (Table 1). When considering the TGA profiles performed in air (Figures S2 and S3) and the results reported in Table 1, the water content within the catalysts is drastically diminishing through the reduction treatment. This effect is expected as zero-valent metals are less hydroscopic than their oxide analogues bearing –OH pending groups at their outer surfaces involving hydrogen-bounds with water molecules.

To assess the potential presence of phases other than Cu° not detectable through X-ray diffractions for the catalyst bearing the bigger copper-based particles (MUB-103(3)), XPS investigations have been performed to finely express the oxidation state of the copper species. Considering the Figure 8, the $Cu2p_{3/2}$ range extends from 930 to 946 eV with main photoelectron peak from 930 to 938 eV and satellite peaks from 938 to 946 eV (Figure 8A).

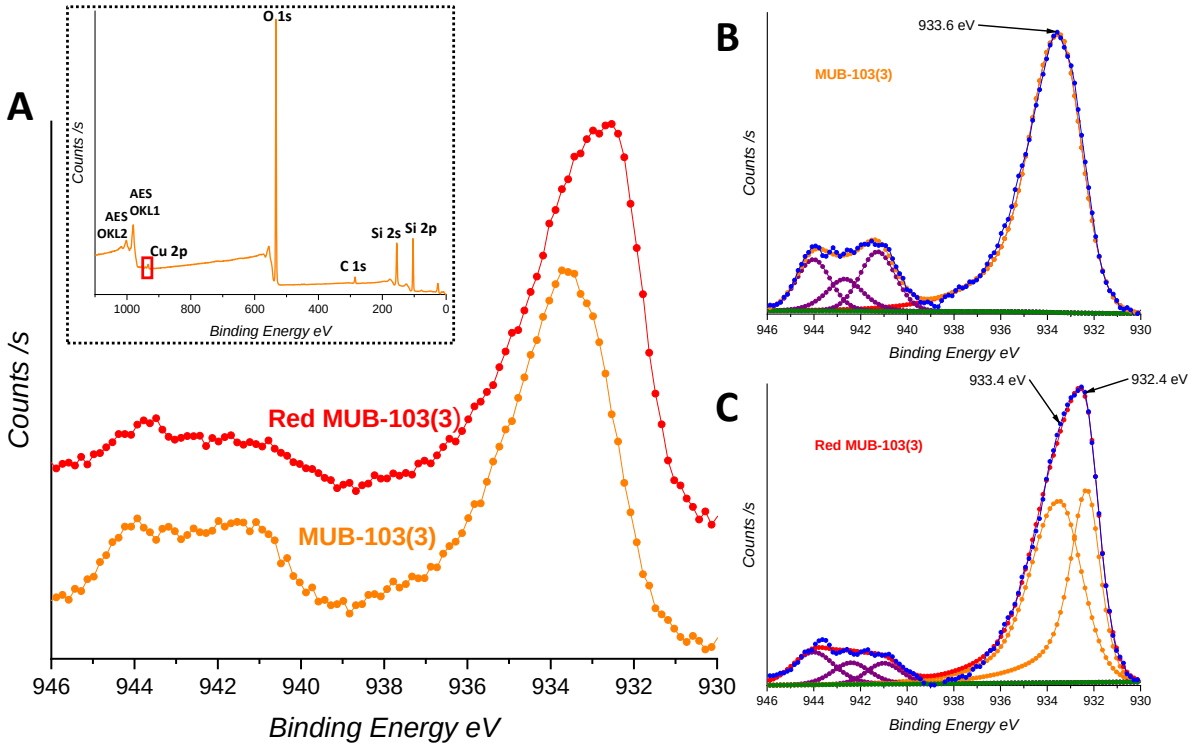


**Figure 8.** XPS spectra of MUB-103(3) and Red MUB-103(3): A) typical survey bearing the Cu 2p location (red rectangular) and corresponding high-resolution Cu $2p_{3/2}$ spectra, B, C) fitted $Cu2p_{3/2}$ spectra.

Fitted spectra for MUB-103(3) and Red MUB-103(3) (Figures 8B and 8C) exhibit some differences, namely: (i) a $Cu^{2+}$ signature for MUB-103(3) in agreement with the WAXS data (Figure 7A) and (ii) a change in the "satellite/main photoelectron" intensities ratio for Red MUB-103(3) explained by a decrease of the $Cu^{2+}$ bonds and an increase of some $Cu_2O$ or $Cu^0$ environments (component at 932.4 eV). WAXS results have already confirmed $Cu^0$ species on Red MUB-103(3) (Figure 7B). However, concerning the Red MUB-103 series the possibility of the presence of $Cu^{1+}$ in addition to Cu° cannot be assessed with certainties under XPS investigations solely. In order to provide a clear cut answer towards the $Cu^{1+}$ species hypothetical presence, TEM-TED analyses were therefore carried out, revealing few additional isolated $Cu_2O$ entities in Red MUB-103(3) material (Figure S6A). Considering the Cu $2p_{3/2}$ XPS fit of the Red MUB-103(2) material we can notice clearly two main components: 933.5 eV characteristic of $Cu^{2+}$ (CuO) and a second one at 932.2 eV associated either with $Cu^{1+}$ ($Cu_2O$) or Cu°. To clear cut this scenario TEM-TED analyses were therefore carried out also with this catalyst, revealing only Cu° particles (Figure S6B). Moreover, when considering the TGA curves of Figures S2 and S3, we can notice that the oxidation of the copper zero valent particles is starting at 183°C falling in the temperature range expected for copper nanoparticles oxidation.[35]

The TPR profiles obtained during the reduction of the MUB-103(x) materials are reported in Figure S7. Two well defined peaks appear for the sample with the highest Cu content (5 wt%, MUB-103(3)) with maxima located at 270 and 330°C, respectively. Such a profile may imply the presence of CuO species with different average sizes on this sample, with the reduction of the smallest CuO nanoparticles around 270°C and of the largest at 330°C, knowing that larger CuO size leads generally to higher reduction temperature in $H_2$-TPR.[36,37] The presence of large CuO nanoparticles on this sample is in accordance both with SEM pictures (Fig. 1f,g), with the TEM data (Fig. 4e,g) and with those of SAXS (Fig. 5).

With the decrease of the Cu loading to 1.65 wt% (MUB-103(2)) and 0.54 wt% (MUB-103(1)), the $H_2$ consumption remains in the same temperature range, from 200°C up to 440°C, with two maxima at 342 and 357°C, respectively, and a shoulder at lower temperature. As only small CuO nanoparticles are present on these two samples, the shift of the temperature of the main peak towards higher temperature with the decrease of the Cu content could reveal an increase of the interaction between the CuO phase and the silica support. The $H_2$ consumption deduced from the TPR profiles (81, 237 and 446 µmol $H_2$ $g^{-1}_{catalyst}$ for MUB-103(1), MUB-103(2) and MUB-103(3) catalysts, respectively) appears in agreement with the theoretical quantity necessary to reduce to Cu° all the CuO phase contained in the two lowest loaded Cu samples (85 and 260 µmol CuO $g^{-1}_{catalyst}$, respectively, considering the stoichiometry given in Table 1), while this consumption remains inferior to the expected quantity for the MUB-103(3) sample (787 µmol CuO $g^{-1}_{catalyst}$). As expressed before, both XPS and TEM-TED analyses of the Red MUB-103(3) catalyst are revealing that this material is not fully reduced with the presence still of $Cu_2O$ entities.

The variation of the CO oxidation catalytic activity as function of the reaction temperature was investigated in the 25-500°C range, using a $CO/O_2$ ratio maintained to 0.4, knowing the adsorption of $O_2$ molecules is strongest compared to CO at the surface of the copper.[5,38] The evolution of the CO conversion with temperature obtained for each MUB-103(x) and Red MUB-103(x) material is given in Fig. 9A. The catalytic performances were also compared in terms of specific activity in Fig. 9B corresponding to the molar quantity of CO converted to $CO_2$ per second and per gram of Cu contained in the sample.

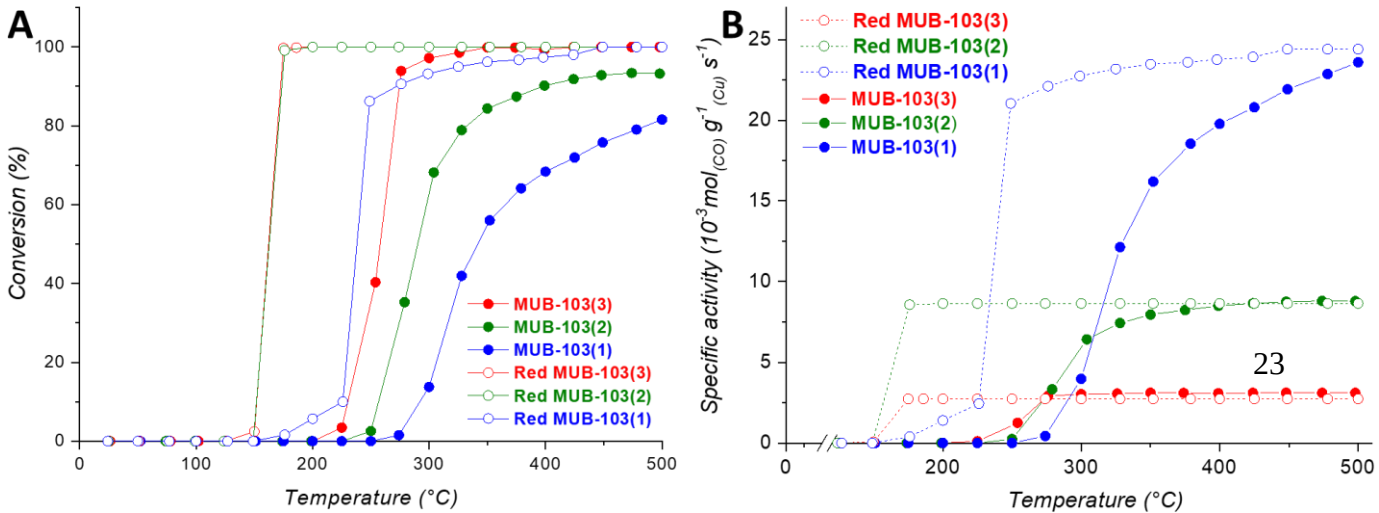

**Figure 9**. A) CO conversion (%) *vs* temperature for MUB-103(1) (plain blue dots), MUB-103(2) (plain green dots), MUB-103(3) (plain red dots) and Red MUB-103(1) (blue circles), Red MUB-103(2) (green circles) and Red MUB-103(3) (red circles). B) Specific activity *vs* temperature for MUB-103(1) (plain blue dots), MUB-103(2) (plain green dots), MUB-103(3) (plain red dots) and Red MUB-103(1) (blue circles), Red MUB-103(2) (green circles) and Red MUB-103(3) (red circles). Standard deviations for conversion 2% and specific activity 2.5%.

For the non-reduced MUB-103(x) series, the increase in the Cu content involves a decrease in the light-off temperature $T_{50}$ (corresponding to 50% of conversion) as follows: 340°C (MUB-103(1)) > 285°C (MUB-103(2)) > 260°C (MUB-103(3)). For the sample with the lowest Cu content, the CO conversion is not total at 500°C reaching 82%. Nevertheless, the catalytic performances exhibited by the CuO phase dispersed in the silica hierarchical porosity of the MUB-103(x) samples appear more efficient for CO oxidation than their $Cu/SiO_2$ mesoporous counterparts, as illustrated in Table 4 comparing the light-off temperature of our samples with that of reported $Cu/SiO_2$ catalysts. For instance, Wang *et al.* evaluated the properties of 3 wt% $Cu/SiO_2$ synthesized *via* deposition-precipitation and pretreated with $O_2$, and obtained in their experimental conditions (2% CO/1% $O_2$/97% He, WHSV of 18,000 mL $h^{-1}$ $g_{cat}^{-1}$) below 10% CO conversion at 300°C, that is to say a lower conversion value than for MUB-103(1) catalyst containing only 0.54 wt% Cu and that despite the use of a lower gas hourly space velocity than in the present study (WHSV = 120,000 mL $h^{-1}$ $g_{cat}^{-1}$), which may be explained by a high $CO/O_2$ ratio.[39] With a WHSV value more than twenty times lower than in our case associated to a $CO/O_2$ ratio extremely low (0.12 compared to 0.4 in this study), Gonçalves *et al.* obtained a light-off temperature of 185°C with a 1.2 wt% $Cu/SiO_2$ oxidized catalyst prepared by magnetron sputtering deposition of copper nanoparticles onto the surface of silica nanopowder.[10] These authors calculated a specific rate equal to 3.78 mmol $g_{Cu}^{-1}$ $s^{-1}$ for around 80% CO conversion on their $Cu/SiO_2$

sample, rate largely exceeded with the MUB-103(2) catalyst after 275°C, *i.e.* from 50% CO conversion (Fig. 9B).

**Table 4.** Light-off temperatures obtained during CO oxidation with $Cu/SiO_2$ catalysts (unreduced or reduced before the test) referenced in the literature, according to the indicated reaction conditions.

| Catalysts | $T_{50}$°C | Reaction conditions | Ref. |
|---|---|---|---|
| 1.2 wt% $Cu/SiO_2$ *unreduced* | 185°C | 1.75% CO/15% $O_2$/83.25% He WHSV 5,2500 $mL.h^{-1}.g_{cat}^{-1}$ | [10] |
| 3 wt% $Cu/SiO_2$ *unreduced* | conversion < 10% at 300°C ($T_{max}$ during the test) | 2% CO/1% $O_2$/97% He WHSV 18,000 $mL.h^{-1}.g_{cat}^{-1}$ | [39] |
| 4.7 wt% Cu/SBA-15 *unreduced* | 260°C | 1% CO/1% $O_2$/98% He WHSV 20,000 $mL.h^{-1}.g_{cat}^{-1}$ | [40] |
| 1.0 wt% Cu/SBA-15 *reduced* | 70°C | 1% CO/99% Air WHSV 7,000 $mL.h^{-1}.g_{cat}^{-1}$ | [42] |
| MUB-103(1) | 340°C | | |
| MUB-103(2) | 285°C | | |
| MUB-103(3) | 260°C | 11.6% CO/29% $O_2$/59.4% $N_2$ | This |
| Red MUB-103(1) | 235°C | WHSV 120,000 $mL.h^{-1}.g_{cat}^{-1}$ | work |
| Red MUB-103(2) | 160°C | | |
| Red MUB-103(3) | 160°C | | |

After reduction with $H_2$ of the MUB-103(x) catalysts, the CO conversion efficiencies significantly increase leading to a lowering of the $T_{50}$ values equal to at least 100°C (Fig. 9A). This observed benefic effect of the hydrogen pretreatment is consistent with studies about copper-based catalysts for CO oxidation revealing that the low oxidation state of copper (Cu°) is more conducive to CO oxidation than high oxidation state (CuO).[10,39-41]According to Fig. 9B, the CO conversion firstly increased with Cu loading, the $T_{50}$ temperature being equal to *ca.* 235°C for Red MUB-103(1) sample containing 0.64 wt% Cu, and to 160°C for Red MUB-103(2) with 1.81 wt% Cu. And then, $T_{50}$ remains unchanged with a further increase of the Cu loading to 5.72 wt% corresponding to Red MUB-103(3) sample. This tendency can result from the presence of residual $Cu_2O$ species (less active than Cu°) in this latest catalyst as expressed before with XPS and TEM-TED experiments. Garcia-Cuello *et al.* evaluated the activity of a 1 wt% Cu/SBA-15 reduced catalyst for CO oxidation and observed a 50% conversion at 70°C, but these authors worked with a very low amount of CO in the gas flow

corresponding to a $CO/O_2$ ratio of 0.05, height times smaller than the ratio used in this study (0.4) (Table 4).[42] Finally, very efficient performances for CO oxidation are obtained for the Red MUB-103(2) material displaying a specific rate of 8.6 $mmol_{CO}\ g_{Cu}^{-1}\ s^{-1}$ at 175°C, largely higher than those observed at the same conversion by Gonçalves *et al.* with the 1.2 wt% $Cu/SiO_2$ catalyst treated with $H_2$ (4.3 $mmol_{CO}\ g_{Cu}^{-1}\ s^{-1}$ at 225°C).[10] Shortly after 225°C, the Red MUB-103(1) loading with only 0.64 wt% Cu exhibits even more higher specific activity, exceeding 20 $mmol_{CO}\ g_{Cu}^{-1}\ s^{-1}$.

The thermodynamic stability of the MUB-103(1) and (2) catalysts evaluated while cycling (Figs. 10A and 10B respectively, the catalysts not having undergone any heat treatment between each cycle) indicates in both case a non-negligible improvement of the CO conversion between the first and second cycle, and a perfect stability for the two further cycles. The decrease in the oxidation temperature profile from the first to the second cycle may result from a beneficial restructuration of the Cu° phase of the Red MUB-103(1) and (2) samples in the course of the CO oxidation process, *i.e.* an increase of the accessibility to the active sites. This behavior may result from a modification of the surface state of the Cu° phase induced during the first temperature rise cycle.

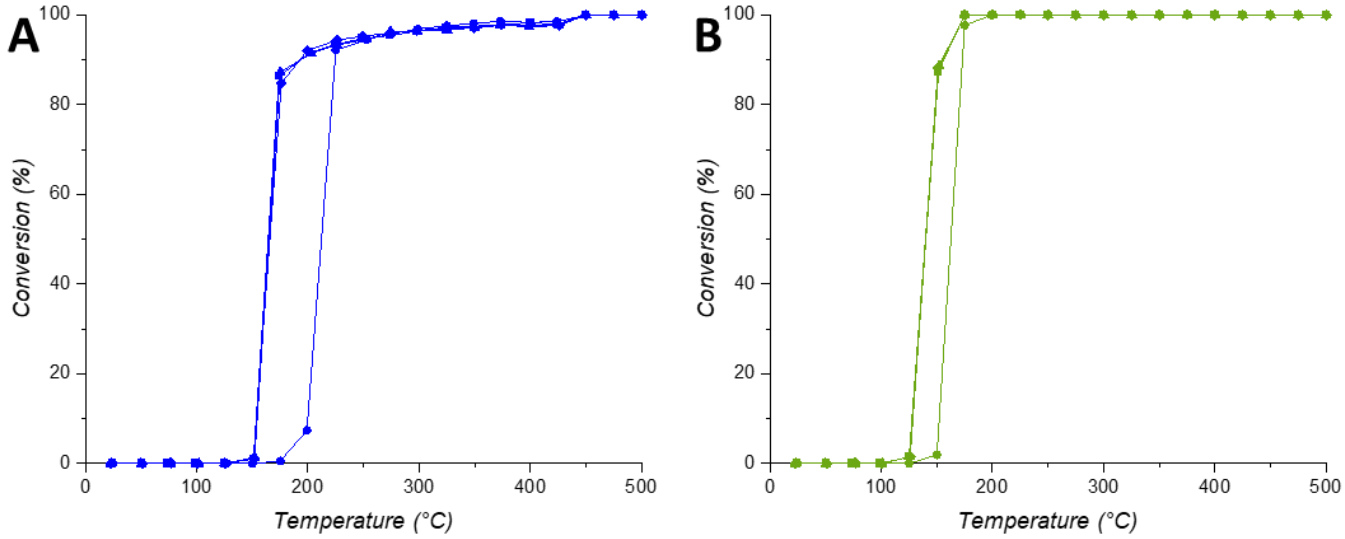


**Figure 10.** CO conversion (%) *vs* temperature for A) Red MUB-103(1) and B) Red MUB-103(2) catalysts during four consecutive cycles: cycle 1 (circles), cycle 2 (triangles), cycle 3 (squares) and cycle 4 (lozenges). Cycles 2, 3 and 4 are super-imposed, thereby hardly distinguishable. Standard deviation for conversion 2%.

Finally, the performances of the Red MUB-103(2) sample were evaluated for CO oxidation in humid condition with the addition of 5 vol% of water vapor in the feed during 4 cycles (Fig. 11). Between each cycle, no heat treatment was performed and the sample was let under the humid gaseous flow during the decrease of the temperature until 100°C (initial temperature of each cycle). The profiles of the conversion curves in Fig. 11 corresponding to cycle 1 then to cycles 2 and 3 appear very similar to those of Fig. 10B, that indicates the Red MUB-103(2) material displays the same catalytic performances with or without the presence of water vapor during the three first cycles (representing a total duration of around 4 h under humid conditions). But a drastic increase of the CO conversion temperature was observed for the cycle 4, *i.e.* after 8 h under humid conditions, with a shift of the $T_{50}$ value beyond 225°C and a CO conversion that remains not total. After the fourth cycle, the deactivated Red MUB-103(2) catalyst was able to partially recover its performances when submitted to a reducing treatment under $H_2$ at 400°C (during 2 h), while a thermal treatment only with $N_2$ at 500°C (during 2 h) was inefficient towards the catalyst regeneration (Fig. S8).

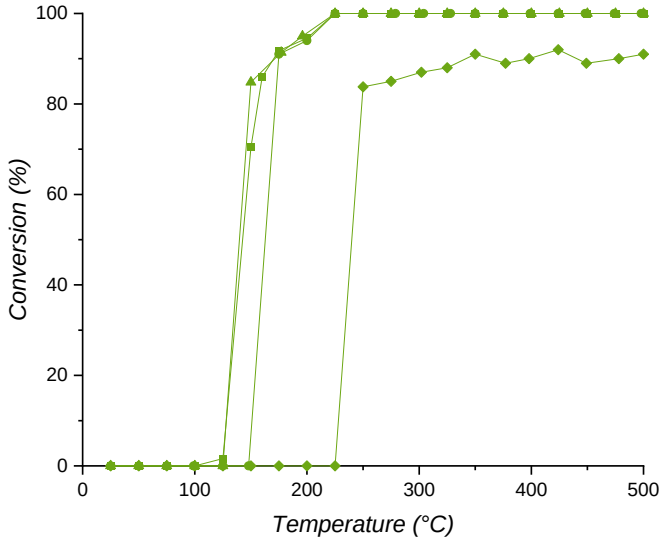


**Figure 11**. CO conversion (%) *vs* temperature in humid conditions (5 vol% water) for Red MUB-103(2) catalyst: cycle 1 (circles), cycle 2 (triangles), cycle 3 (squares) and cycle 4 (lozenges). Standard deviation for conversion 2%.

We investigated the spent Red MUB-103(2) catalyst to estimate the reason for the decreasing efficiency in humid conditions for CO oxidation when cycling (Multicycles MC). WAXS investigation highlights the oxidation state to $Cu^{2+}$ under the CuO Miller indices signature (Figure S9, red bottom). To get further finely insight, TEM-TED experiment was also performed, revealing isolated particles of $Cu_2O$, but also remaining Cu° (Figure S6C). The deactivation can then be attributed to this partial oxidation of the zero valent copper phase.

We have also investigated the behavior of the Red MUB-103(2) catalyst during a long cycle (LC) of CO oxidation performed during 6 h under isothermal conditions (at 175°C) either in dry or humid conditions (5 vol% water) (Figure S10). In both cases, the CO conversion decreases gradually as function of time, in a more intense way in presence of water in the gaseous flow. WAXS investigation depict a rather amorphous pattern where weak CuO diffraction peaks can be barely distinguished (Figure S9, blue top). To get further insight into the surface composition and chemical states of the Red MUB-103(2) material

after this long cycle under humid conditions, we performed X-ray photoelectron spectroscopy investigations (XPS), indicating that the long catalytic process induced a slight oxidation of copper towards CuO (Figure S11) detrimental on the catalytic performances. To complement, TEM-TED experiment revealed additional isolated particles of $Cu_2O$ (Figure S6D).

## 4. CONCLUSIONS

In the course of this study though the integration[43] of complex fluids and sol-gel chemistry, copper-based self-standing monoliths catalyst bearing hierarchical porosity and polydisperse copper-based nano-micro-particles have been obtained. Both the native copper oxide based catalysts (MUB-103(x)) and their reduced homologues (Red MUB-103(x)) have been characterized at various length scale as well as tested towards the thermo-conversion of CO towards $CO_2$ in dried air, revealing that for the non-reduced catalysts an increase in the Cu content promotes a decrease in the light-off temperature $T_{50}$ (corresponding to 50% of conversion) as follows: 340°C (MUB-103(1)) > 285°C (MUB-103(2)) > 260°C (MUB-103(3)). The catalytic performances exhibited by the CuO phase dispersed in the silica porosity of the MUB-103(x) samples are the highest reached to date despite the penalty of using here a higher gas hourly space velocity. After reduction with $H_2$ of the MUB-103(x) catalysts, the CO conversion efficiencies significantly increase leading to a lowering of the $T_{50}$ values equal to at least 100°C. Once reduced and considering the Red MUB-103(x) series, the CO conversion firstly increased with Cu loading, the $T_{50}$ temperature being equal to *ca.* 235°C for Red MUB-103(1) sample containing 0.64 wt% Cu, and to 160°C for Red MUB-103(2) with 1.81 wt% Cu. And then, $T_{50}$ remains unchanged with a further increase of the Cu loading to 5.72 wt% corresponding to Red MUB-103(3) sample. Very efficient performances for CO oxidation are obtained for the Red MUB-103(2) material displaying a specific rate of 8.6 $mmol_{CO}\ g_{Cu}^{-1}\ s^{-1}$ at 175°C, largely higher than those observed in the literature, with a very

good stability during 4 consecutive CO oxidation cycles. The performances of the Red MUB-103(2) sample were also evaluated during 4 cycles in humid conditions with the addition of 5 vol% of water vapor in the feed. No influence of the presence of water vapor was observed on the three first cycles (representing a total duration of around 4 h under humid conditions) but a drastic increase of the CO conversion temperature was observed for the 4$^{th}$ cycle, *i.e.* after 8 h under humid conditions, with a shift of the $T_{50}$ value beyond 225°C and a CO conversion that remains not total. Analyses of the spent Red MUB-103(2) catalyst after 4 cycles under humid conditions reveal a slight oxidation of copper, leading to $Cu_2O$ species detrimental on the catalytic performances. After these four cycles, the deactivated catalyst was able to partially recover its performances when reactivated through a reducing treatment under $H_2$ at 400°C (during 2 h). The gradual oxidation of the Cu° phase of the Red MUB-103(2) catalyst under humid conditions was also put in evidence during a long CO conversion test (6 h reaction time) performed in isothermal conditions at 175°C.

## ASSOCIATED CONTENT

Supporting Information is available free of charge at https://xxxxxxxxxxxxxxxxxxxxxxxxxxxxxxxxxxxxxxxxxxxxxxxx

SEM investigation over the Red MUB-103(x) series, TGA experiments, XPS investigations, TEM-TED coupled analyses, TRP profiles, WAXS investigations over the spent catalysts, CO conversion in humid condition for the spent Red MUB-103(2) catalyst after reactivation, CO conversion for the Red MUB-103(2) catalyst during a long CO conversion test (6 h) at 175°C (PDF).

## AUTHOR INFORMATION

### Corresponding Authors

**Rénal Backov** - Université de Bordeaux, CRPP-UMR CNRS 5031, 115 Avenue Albert Schweitzer, 33600 Pessac, France. https://orcid.org/0000-0001-5946-8917 ; E-mail: renal.backov@crpp.cnrs.fr

**Catherine Especel** - Institut de Chimie des Milieux et Matériaux de Poitiers (IC2MP), UMR 7285 CNRS - Université de Poitiers, 4 rue Michel Brunet, TSA 51106, 86073 Poitiers Cedex 9 – France. https://orcid.org/0000-0002-4066-6515 ; E-mail: catherine.especel@univ-poitiers.fr

## Authors

**Antoine Vardon -** Université de Bordeaux, CRPP-UMR CNRS 5031, 115 Avenue Albert Schweitzer, 33600 Pessac, France.
.https://orcid.org/0000-0002-3182-5879

**Hugo Labarrère -** Université de Bordeaux, CRPP-UMR CNRS 5031, 115 Avenue Albert Schweitzer, 33600 Pessac, France.

**Nicolas Chanut -** Massachusetts Institute of Technology, Department of Civil and Environmental Engineering, 77, Mass. Avenue, Cambridge MA 02139, USA.
https://orcid.org/0000-0002-5159-9901

**François Weill -** Université de Bordeaux, Bordeaux INP**,** ICMCB-UMR CNRS 5026, 87 Avenue Albert Schweitzer, F-33600 Pessac, France.
https://orcid.org/0000-0001-8331-6075

**Christine Labrugère-Sarroste -** Université de Bordeaux, PLACAMAT-UAR CNRS 3626, 87 Avenue Albert Schweitzer, F-33600 Pessac, France.

**Jean-Louis Bobet -** Université de Bordeaux, ICMCB-UMR CNRS 5026, 87 Avenue Albert Schweitzer, F-33600 Pessac, France.
https://orcid.org/0000-0001-7838-7004

**Florence Epron** - Institut de Chimie des Milieux et Matériaux de Poitiers (IC2MP), UMR 7285 CNRS - Université de Poitiers, 4 rue Michel Brunet, TSA 51106, 86073 Poitiers Cedex 9 – France.
https://orcid.org/0000-0002-7720-1578

**Author contributions**

The manuscript was written through contributions of all authors. All authors have given approval to the final version of the manuscript.

**Notes**

The authors declare no competing financial interest.

**ACKNOWLEGMENTS**

R.B. wishes to thank Dr. Marie-Anne Dourges for the poro-mercury data acquisitions, Sabrina Lacomme (Bordeaux Imaging Center- BIC) for the TEM investigations and Ahmed Bentaleb for both SAXS and WAXS acquisitions data. The authors wish to thank the CNRS, the University of Bordeaux, the Région "Nouvelle Aquitaine" and the European Union (ERDF). C.E. wishes to thank Meriem Chennoufi (Master degree trainee) and Joudia Akil (Engineer) for acquiring the CO oxidation data sets.

## REFERENCES

(1) Li, P.; Miser, D.E.; Rabiei, S.; Yadav, R.T.; Hajaligol, M.R. The removal of carbon monoxide by iron oxide nanoparticles. *Appl Catal, B.* **2003**, *43*, 151–162.

(2) Carlsson, P.A.; Skoglundh, M. Low-temperature oxidation of carbon monoxide and methane over alumina and ceria supported platinum catalysts. *Appl Catal, B.* **2011**, 101:669–675.

(3) Judai, K.; Abbet, S.; Wörz, A.S.; Heiz, U.; Henry, C.R. Low-temperature cluster catalysis. J *Am Chem Soc.* **2004**, *126*, 2732–2737.

(4) Manjula, P.; Arunkumar, S.; Manorama, S.V. Au/$SnO_2$ an excellent material for room temperature CO sensing. *Sens Actu B.* **2011**, 152, 168–175.

(5) Royer, S.; Duprez, D. Catalytic oxidation of CO over transition metal oxides. *Chem Cat Chem.* **2011**; *3*, 24–65.

(6) Kaspar, J.; Fornasiero, P.; Hickey, N. Automotive catalytic converters: Current status and some perspectives. *Catal. Today* **2003**, *77*, 419–449.

(7) Pillai, U. R.; Deevi, S. Room Temperature Oxidation of Carbon Monoxide Over Copper Oxide Catalyst. *Appl. Catal. B: Environ*. **2006**, *64*, 146−151.

(8) White, B.; Yin, M.; Hall, A.; Le, D.; Stolbov, S.; Rahman, T.; Turro, N.; O'Brien, S. Complete CO Oxidation over $Cu_2O$ Nanoparticles Supported on Silica Gel. *Nano Lett*. **2006**, *6*, 2095−2098.

(9) Wu, G.; Guan, N.; Li, L. Low Temperature CO Oxidation on Cu- $Cu_2O/TiO_2$ Catalyst Prepared by Photodeposition. *Catal. Sci. Tech* **2011**, *1*, 601−608.

(10) Gonçalves, R.V.; Wojcieszak, R.; Wender, H.; Dias, C.S.B.; Vono, L.L.R, Eberhardt, D.; Teixeira, S.R.; Rossi, L. M. Easy Access to Metallic Copper Nanoparticles with High Activity and Stability for CO Oxidation. *ACS Appl. Mater. Interfaces* **2015**, *7*, 7987−7994

(11) Avhad, M.; Flaud, V.; Burel, L.; Cavailles, J.; Sakpal, T.; Lefferts, L.; Kaper, H. Porous carbon as catalyst support for CO oxidation: Impact of nitrogen doping. *Carbon* **2020**, *169*, 297−306

(12) Li, H.; Shen, M.; Wang, J.; Wang, H.; Wang, J. Effect of Support on CO Oxidation Performance over the Pd/$CeO_2$ and Pd/$CeO_2$–$ZrO_2$ Catalyst. *Ind. Eng. Chem. Res*. **2020**, *59*, 4, 1477−1486.

(13) Silverstein, M. S. Recent advances in emulsion-templated porous polymers. *Prog. Polym. Sci.* **2014**, *39*, 199−234.

(14) Silverstein, M. S. Emulsion-templated polymers: Contemporary contemplations. *Polymer* **2017**, *126*, 261−282.

(15) Silverstein, M. S. The Chemistry of Porous Polymers: The Holy Grail. *Israel. J. Chem.* **2020**, *60*, 140−150.

(16) Araya, A. Hydrophobic, Highly Porous, Three-Dimensional Inorganic Structures. *US Patent 4888309*, **1989**.

(17) Carn, F.; Colin, A.; Achard, M.-F.; Deleuze, H.; Sellier, E.; Birot, M.; Backov, R. Inorganic monoliths hierarchically textured via concentrated direct emulsion and micellar templates. *J. Mater. Chem*. **2004**, 14, 1370−1376.

(18) Brun, N.; Ungureanu, S.; Deleuze, H.; Backov, R. Hybrid foams, colloids and beyond: From design to applications. *Chem. Soc. Rev.* **2011**, *40*, 771−788.

(19) Roucher, A.; Depardieu, M.; Pekin, D.; Morvan, M.; Backov, R. Inorganic, hybridized and living macrocellular foams: "Out of the Box" heterogeneous catalysis. *Chem. Record.* **2018**, *18*, 776−787.

(20) Roucher, A.; Morvan, M.; Pekin, D.; Depardieu, M.; Blin, J.-L.; Schmitt, V.; Baret, J.-C.; Backov, R. From Compartmentalization of Bacteria within Inorganic Macrocellular Beads to the Assembly of Microbial Consortia. *Adv. Biosystems* **2018**, *2*, 201700233.

(21) Brun, N.; Babeau-Garcia, A.; Achard, M.-F.; Sanchez, C.; Durand, F.; Guillaume, L.; Birot, M.; Deleuze, H.; Backov, R. Enzyme-Based Biohybrid Foams Designed for Continuous Flow Heterogeneous Catalysis and Biodiesel Production. *Energy § Environmental Science* **2011**, *4*, 2840−2844.

(22) Gaikwad, P.; Ungureanu, S.; Backov, R.; Vynck, K.; Vallée, R.A.L. Photon transport in cylindrically-shaped disordered meso-macroporous materials. *Optic Express* **2014**, *22*, 7503−7513.

(23) Bachelard, N.; Gaikwad, P.; Backov, R.; Sebbah, P.; Vallée, R.A.L. Disorder as a Playground for the Coexistence of Optical Nonlinear Effects: Competition between Random

Lasing and Stimulated Raman Scattering in Complex Porous Materials. *ACS Photonics* **2014**, *1*, 1206−1211.

(24) Gaikwad, P.; Bachelar, N.; Sebbah, P.; Backov, R.; Vallée, R.A.L. Competition and Coexistence of Raman and Random Lasing in Silica-Titania-Based Solid Foams. *Adv. Optical Mater*. **2015**, *3*, 1640−1651.

(25) Bernadet, S.; Tavernier, E.; Ta, D.-M.; Vallée, R.A.L.; Ravaine, S.; Fécant A.; Backov, R. Bulk Photo-Driven $CO_2$ Conversion through $TiO_2$@Si(HIPE) Monolithic Macrocellular Foams. *Adv. Funct Mat.* **2019**, *29*, 1807767.

(26) Debecker, D. P.; Boissière, C.; Guillaume, L.; Huet, S.; Eliaers, P.; Sanchez, C.; Backov, R. First acidic macro-mesocellular aluminosilicate monolithic foams "SiAl(HIPE)" and their catalytic properties. *Chem. Commun*. **2015**, *51*, 14018−14021.

(27) Roucher, A.; Bentaleb, A.; Laurichesse, E.; Dourges, M.-A.; Emo, M.; Schmitt, V.; Blin, J.-L.; Backov, R. First Macro-Mesocellular Silica SBA-15-Si(HIPE) Monoliths: Conditions for Obtaining Self-Standing Materials. *Chem. Mater*. **2018**, *30*, 864−873.

(28) Roucher, A.; Emo, M.; Vibert, F.; Stébé, M-J.; Schmitt, V.; Jonas, F.; Backov, R.; Blin, J-L. Investigation of mixed ionic/nonionic building blocks for the dual templating of macro-mesoporous silica foams. *J. Coll. Inter. Sci*. **2019**, *533*, 385−400.

(29) Ly, I.; Vardon, A.; Chanut, N.; Nallet, F.; Pellenq, R. J.-M.; Rouzières, M.; Clérac, R.; Akil, J.; Epron, F.; Especel, C.; Backov, R. Binary CoOx–$SiO_2$ Porous Nanostructures for Catalytic CO Oxidation. *ACS Appl. Nano Mater*. **2022**, *5*, 7331–7343.

(30) Brunauer, S.; Emmett, P. H.; Teller, E. Adsorption of Gases in Multimolecular Layers. *J. Am. Chem. Soc.* **1938**, *60*, 309–319.

(31) Brinker, C.J.; Scherer, G.W. "*Sol-Gel Science: The Physics and Chemistry of Sol-Gel Processing",* Academic Press, INC, **1990,** 908 p.

(32) Zangi, R. Can Salting-in/Salting-out Ions Be Classified as Chaotropes/Kosmotropes? *J. Phys. Chem. B*, **2010**, *114*, 643–650.

(33) Poyraz, A.S.; Dag, Ö. Role of Organic and Inorganic Additives on the Assembly of CTAB-P123 and the Morphology of Mesoporous Silica Particles. *J. Phys. Chem. C*. **2009**, *113*, 18596–18607.

(34) Porod, G., "*Small Angle X-ray Scattering: General theory*", Glatter, O.; Kratky, O. (Eds), Academic Press, London, **1982,** 515 p.

(35) Yabuki, A.; Tanaka, S. Oxidation behavior of copper nanoparticles at low temperature, *Mat. Res. Bull*. **2011**, *46*, 2323−2327.

(36) Zheng, X.-C.; Wu, S.-H.; Wang, S.-P.; Wang, S.-R.; Zhang, S.-M.; Huang, W.-P. The Preparation and Catalytic Behavior of Copper−Cerium Oxide Catalysts for Low-Temperature Carbon Monoxide Oxidation. *Appl. Catal. A* **2005**, *283*, 217−223.

(37) Liu, Z.; Amiridis, M. D.; Chen, Y. Characterization of CuO Supported on Tetragonal $ZrO_2$ Catalysts for $N_2O$ Decomposition to $N_2$. J. *Phys. Chem. B* **2005**, *109*, 1251−1255.

(38) Choi K.I.; Vannice M.A. CO oxidation over Pd and Cu catalysts IV. Prereduced $Al_2O_3$-supported copper. *J. Catal.* **1991**, *131*, 22-35.

(39) Wang M-M.; Yu J.; Wang W-W.; Chen J-X.; Jia C-J.; Si R. Effects of Hydrogen and Hydrothermal Preatreatments on a Silica-Supported Copper Catalyst for CO oxidation: Copper Hydroxy Active Species, *J. Phys. Chem. C.* **2020**, *124*, 25270–25281.

(40) Tu C-H.; Wang A-Q.; Zheng M-Y.; Wang X-D.; Zhang T. Factors influencing the catalytic activity of SBA-15- supported copper nanoparticles in CO oxidation, *Appl. Catal. A: Gen.* **2006**, *297*, 40–47.

(41) Xu F.; Mudiyanselage K.; Baber A.E.; Soldemo M.; Weissenreider J.; White M.G.; Stacchiola D.J. Redox-Mediated Reconstruction of Copper during Carbon Monoxide Oxidation, *J. Phys. Chem. C.* **2014**, *118*, 15902–15909.

(42) Garcia-Cuello V.S.; Giraldo L.; Moreno-Piraján C. Synthesis, Characterization, and Application in the CO Oxidation over a Copper Nanocatalyst Confined in SBA-15, *J. Chem. Eng. Data* **2011**, *56*, 1167–1173.

(43) Backov, R. Combining soft matter and soft chemistry: integrative chemistry towards designing novel and complex multiscale architectures. *Soft Matter*. **2006**, *2*, 452–464.

**TOC**

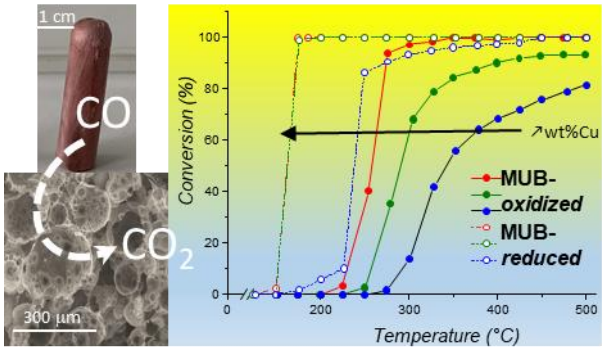
1 cm
CO
$CO_2$
300 µm
Conversion (%)
Temperature (°C)
↗wt%Cu
MUB-
oxidized
MUB-
reduced